Revisiting high-frequency oscillatory ventilation *in vitro* and *in silico* in neonatal conductive airways

Katrin Bauer[a], Eliram Nof[b], Josué Sznitman[b],*

[a] *Institute of Mechanics and Fluid Dynamics, TU Bergakademie Freiberg, 09599 Freiberg, Germany*
[b] *Department of Biomedical Engineering, Technion — Israel Institute of Technology, Haifa 32000, Israel*

ARTICLE INFO

ABSTRACT

Background: High frequency oscillatory ventilation is often used for lung support in premature neonates suffering from respiratory distress syndrome. Despite its broad use in neonatal intensive care units, there are to date no accepted protocols for the choice of appropriate ventilation parameter settings. In this context, the underlying mass transport mechanisms are still not fully understood.
Methods: We revisit the question of flow phenomena under conventional mechanical ventilation and high frequency oscillatory ventilation in an anatomically-inspired model of neonatal conductive airways spanning the first few airway generations. We first perform at true scale *in vitro* particle image velocimetry measurements of respiratory flow patterns. Next, we explore *in silico* convective mass transport in computational fluid dynamics simulations by implementing Lagrangian tracking of tracer boli, where the ventilatory flow rate is fixed.
Findings: Particle image velocimetry measurements at eight representative phase angles of a breathing cycle reveal similar flow patterns at peak velocity and during deceleration phases for conventional mechanical ventilation and high frequency oscillatory ventilation. Characteristic differences occur during the acceleration and flow reversal phases. Net displacements of the tracer particles rapidly reach asymptotic behaviour over cumulative breathing cycles and suggest a linear relation between tidal volume and convective mass transport.
Interpretation: The linear relation observed suggests that differences in flow characteristics between conventional mechanical ventilation and high frequency oscillatory ventilation conditions do not substantially influence convective mass transport mechanisms. Lower tidal volumes thus cannot be compensated straightforwardly by selecting higher frequencies to maintain similar ventilation efficiencies.

1. Introduction

Premature born neonates often need ventilatory assistance during their first days of life. Their immature lungs may suffer from respiratory distress syndrome (RDS), where a deficiency of pulmonary surfactant in the alveolar space renders the act of breathing strenuous if not compromised. In particular, regions of the airspace are closed or collapsed (i.e. atelectasis) while others are overstretched. To address such needs, neonatal lungs require a "protective ventilation" strategy by reopening collapsed regions while preventing overstretching of healthy regions (Nieman et al., 2017). The challenge of both rescue therapy and ventilatory support is thus to guarantee breathing without damaging the lungs and avoid adverse effects on long term health (Gerstmann et al., 2001). In this context, traditional methods relying on conventional mechanical ventilation (CMV) have often been associated with ventilator-induced lung injury (VILI), including baro- and volutrauma (Slutsky and Ranieri, 2013; Whitehead, 2002).

One alternative approach that has shown to curtail such risk factors is high frequency oscillatory ventilation (HFOV); a technique also recently applied non-invasively (De Luca and Dell'Orto, 2016). The underlying principle of HFOV relies on the combination of reduced tidal volumes (V_T) with increased oscillatory frequencies (f). Typical values of tidal volume are in the range of 1–3 ml/kg bodyweight; a volume that represents about 50% or less of the anatomical dead space. Correspondingly, ventilation frequencies are increased to 5–15 Hz, depending on the patient's age (Rimensberger et al., 2015). Despite such low tidal volumes, HFOV is known to sustain sufficient oxygenation and CO_2 elimination (Imai et al., 2001; Stachow, 1995), both of which strongly depend on the adequate combination of ventilation frequency, tidal volume and mean airway pressure (MAP).

Although HFOV has become increasingly common in neonatal intensive care units (NICU), there are to date no widely-accepted protocols for prioritizing the use of HFOV versus CMV in neonatal respiratory failure. Recent studies have even suggested that HFOV should not be

* Corresponding author.
E-mail addresses: Katrin.Bauer@imfd.tu-freiberg.de (K. Bauer), eliram@campus.technion.ac.il (E. Nof), sznitman@bm.technion.ac.il (J. Sznitman).

used preventively as it is not proven to be superior to CMV with respect to mortality rate or neurodevelopmental outcome in preterm babies (Owen et al., 2017). While optimal parameter settings for tidal volume and frequency are known to vary between NICUs, a higher frequency is generally suggested in HFOV for low lung compliance whereas a lower frequency may be better suited for high resistance lungs (Pillow, 2005; Venegas and Fredberg, 1994). It is also suggested that as frequency increases, airflow distribution depends less on compliance but rather on airway resistance and lung inertance (Venegas and Fredberg, 1994).

One of the plausible reasons for ongoing discrepancies in selecting HFOV parameters emanates from the fact that the underlying transport mechanisms in HFOV are still not fully understood. While bulk convection leads to direct alveolar ventilation in CMV (Chang, 1984; Slutsky and Drazen, 2002), gas exchange during HFOV is effectively sustained despite a V_T smaller than the anatomical dead space. This outcome suggests that alternative mechanisms are anticipated to play a role for effective mass transport. For example, the coupling between gas diffusion and a non-uniform axial velocity profile as well as secondary flows has been shown to promote augmented axial dispersion at higher oscillatory frequencies (Kamm, 1989). In parallel, asymmetric velocity patterns that arise between inspiration and expiration are known to cause a net flow also referred to as *steady streaming* (Haselton and Scherer, 1982). This lack of flow reversibility causes fluid to migrate to different axial locations after each cycle (Tanaka et al., 2001). Notably, Han et al. (2016) analysed such streaming behaviour in a planar, symmetric double bifurcation model under CMV and HFOV conditions. They presented numerical results of the net displacement of Lagrangian (fluid) particles, where streaming strongly increased at higher frequencies. Yet, the authors only varied the oscillatory frequency and not the corresponding tidal volume such that the effective ventilation efficiency (Pillow, 2005) was not held constant.

In parallel to such considerations, another widely cited phenomenon is the so-called *pendelluft* effect (Imai et al., 2001; Drazen et al., 1984; Otis et al., 1956), whereby varying time constants of different lung regions lead to asynchronous filling and emptying and therefore local airflows may occur between adjacent airway branches. Choi et al. (2010) observed that during HFOV the counter-flow phenomenon at flow reversal can sustain over a longer period of time and may thus contribute to enhanced flow mixing. More recently, Bauer et al. (2012) visualized mass transport in a human lung model at varying frequencies and attributed pendelluft to a homogenization of mass flow distribution at increasing frequencies. These works support the hypothesis of enhanced convective mixing under HFOV.

Despite such progress, to what extent these transport mechanisms differ from CMV still remains largely unexplored. Moreover, HFOV is often qualitatively characterized as an amalgam of the various flow mixing mechanisms (e.g. turbulence, Taylor dispersion, steady streaming, pendelluft, etc.) without an obvious quantification of the relative importance of each (Imai et al., 2001; Pillow, 2005). Specifically, all aforementioned studies have considered HFOV settings in adult lungs rather than in premature baby anatomies. In the present study, we revisit the question of flow phenomena under CMV and HFOV in an anatomically-inspired idealized model of neonatal conductive airways featuring a planar, symmetric tree spanning the first few airway generations. We begin by investigating in true-scale experiments using particle image velocimetry (PIV) whether underlying respiratory flow topologies fundamentally differ between ventilation strategies. Following validation of our numerical simulations with experimental data, we explore the evolution of passive tracer boli for varying HFOV settings (i.e. combinations of fixed $V_T \times f$). Our efforts deliver new mechanistic insight on the characteristics of convective mass transport in neonatal HFOV and shed some light on identifying the underlying similarities with CMV.
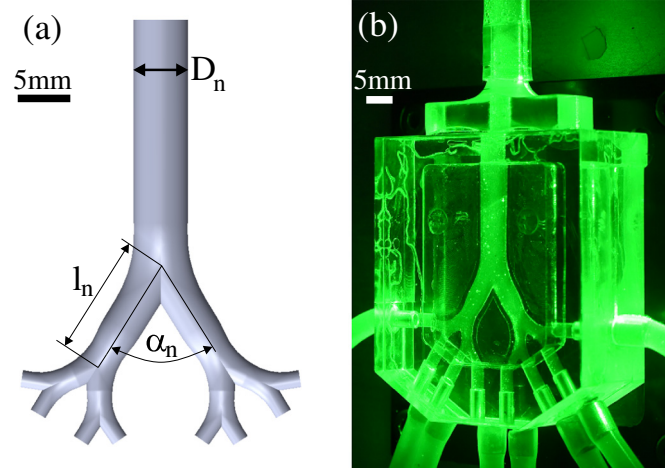

Fig. 1. (a) Computer-aided design (CAD) model and parameters of the neonatal conductive airway model (see corresponding Table 1). (b) Detail of the transparent cast of the conductive airway model seeded with particles and illuminated by a laser light sheet for PIV measurements (see Experimental methods 2.1).

2. Methods

Our experimental and numerical investigations revolve around the use of an anatomically-inspired idealized symmetric neonatal model of upper airways, spanning four generations (Fig. 1a). In the absence of widely-available morphometric data on neonatal lungs, dimensions were adapted from Ménache et al. (2008) for a 3 month old newborn. To recreate generic conductive airways of a premature baby (approximately 2 kg), values from Ménache et al. (2008) were scaled such that the tracheal diameter is 5 mm. Geometrical parameters are summarized in Table 1 where n denotes the generation number, D_n and l_n the corresponding branch diameter and length, respectively and α_n the bifurcating angle of each airway generation. We note that the simplified geometry is planar with circular cross sections; a feature specifically chosen for easiness of planar 2D PIV measurements across the geometry mid-plane (see details below). While the anatomy investigated here does not hence feature out-of-plane branching structures, ensuing flow features are nevertheless asymmetric and three-dimensional (Jalal et al., 2016; Theunissen and Riethmuller, 2008) as a result of inertial (e.g. Dean) flows amongst others (see Results and discussion 3).

2.1. Experimental methods

The experimental mold was manufactured from an aluminum slab using CNC machining from which a cast of the airways was obtained from transparent silicone (Elastosil RT 601, Wacker) and sealed in a Plexiglas chamber to which inlet and outlet tubing were carefully fitted with matching lengths (Fig. 1b). A 42/58 (mass ratio) water/glycerol mixture of density $\rho_f = 1150$ kg/m³ and dynamic viscosity $\mu_f = 9.66 \times 10^{-3}$ kg/m-s is used as the working fluid to match the refractive index of the silicone ($n = 1.4095$). A linear motor (Linmot, PS01-23 ×160H-HP-R, Switzerland) is connected to the trachea (i.e. inlet) which drives the fluid into and out of the model through the

Table 1
Geometrical characteristics of the simplified neonatal upper airways model (see corresponding Fig. 1a).

n	D_n (mm)	l_n (mm)	α_n (deg)
0	5.24	23.8	
1	3.93	11.3	64
2	2.49	4.61	66
3	1.65	3.36	68

Table 2
Comparison of flow parameters under CMV and HFOV conditions. $^{(*)}$ denotes parameters used for experiments. Dn_1 denotes the Dean number in the first daughter generation with the corresponding Reynolds number Re_1.

f (Hz)	V_T (ml)	u_{max} (m/s)	Re_0	α	Re_1	Dn_1
$0.5^{(*)}$	10	0.728	455	1.6	300	122
2	2.5	0.728	225	2.3	160	64
4	1.25	0.728	225	3.3	160	64
$5^{(*)}$	1	0.728	455	5	300	122
5	1	0.728	225	3.7	160	64
10	0.5	0.728	225	5.2	160	64

piston following a prescribed oscillatory motion. Frequency and tidal volume can be freely adjusted to simulate both CMV and HFOV conditions (see Table 2). Note that the distal endings of the (eight) outlet tubing are open to ambient pressure.

Based on the ventilatory scenario reproduced (i.e. combination of V_T and f), the peak Reynolds number during the breathing cycle is given by $Re = 4V_T f \rho_f / D_0 \mu_f$ (at peak velocity in the trachea); the corresponding Womersley number capturing unsteady inertial effects due to oscillatory motion is defined as $\alpha = (D_0/2)\sqrt{2\pi f \rho_f / \mu_f}$. Following dynamic similarity, experimental flow parameters are thus adjusted to match characteristic values of Re and α in both CMV and HFOV (indicated by (*) in Table 2). Note that the Reynolds number for the experiments is larger despite the same peak velocity since the kinematic viscosity of the water-glycerin mixture is only about half of that of air. The Dean number in the main bifurcation is defined as $Dn_1 = Re_1 \sqrt{D_1/2r_1}$, where r_1 denotes the radius of curvature and is summarized in Table 2 for the varying ventilatory settings.

Velocity maps in the airways are extracted using 2D planar Particle Image Velocimetry (PIV), similar to previous studies (Adler and Brücker, 2007; Große et al., 2007). Tracer particles (hollow glass spheres of a mean diameter $d_p = 10\ \mu m$ and density of $\rho = 1100\ kg/m^3$) are seeded in the working fluid and assumed to move with the flow subject to negligible sedimentation. Namely, the residual settling velocity of the particles in the fluid is estimated to be $u_s = \|\rho_p \rho_f\| d_p^2 g / 18 \mu_f \approx 280\ nm/s$, where g is the gravitational acceleration. The particles are illuminated in the model across the symmetry plane by a laser light sheet emitted from a Nd:YAG double-cavity laser (Nano L Litron Lasers; 15 Hz repetition rate), as shown in Fig. 1b.

Triggering of a double shutter CCD camera (with 30 fps; Imager Pro X 2M) in sync with the laser acquires phase-locked double images. Following the time delay between the double images, which was varied between 80 and 1000 μ s according to the peak phase velocity, whole-field velocity vector maps are extracted from a cross-correlation PIV software (Davis, LaVision GmbH, Germany) and phase-locked results are presented as the mean velocity fields from averaging 50 oscillatory cycles.

2.2. Numerical methods

To validate our numerical simulations with PIV measurements, computational fluid dynamics (CFD) simulations were first conducted in the identical conductive airway geometry used in experiments (Fig. 1a). Namely, conservation of mass and momentum (i.e. Navier-Stokes) equations are solved using the Finite Volume Method (FVM) in ANSYS Fluent. Given the range of peak tracheal Reynolds number ($Re_0 < 500$) characteristic of CMV and HFOV conditions mimicked (Table 2), flows remain laminar at all times. Cyclic flow conditions are applied at the inlet (i.e. trachea) as defined in Table 2, where we impose a parabolic, sinusoidal oscillating velocity profile. At each of the eight distal outlets, a zero pressure is employed to mimic the experimental boundary conditions.

The airway model is meshed with tetrahedral cells and a wall prism layer (ANSYS ICEM). Rigorous mesh convergence tests were first

performed to select the optimal numerical setup. Tetrahedral Delaunay meshes ranging between 0.4 M and 3.8 M cells were investigated. In particular, we independently examined the near wall refinements as well as refinements of large airway branches, small branches and high curvature regions. For each of these meshes, mass conservation was verified and velocity values converged to a 0.01% tolerance. Following our convergence tests, the resultant mesh had 0.9 M cells with three near wall prism layers. The convergence error of the selected mesh was below 2% throughout the domain when compared to the finest mesh examined. Subsequently, convergence tests were also used to select the appropriate accuracy of the numerical models. A coupled pressure-velocity scheme was selected along with a Least Squares Cell-Based scheme for the gradients, a second order discretization scheme for the pressure term and Second Order Upwind scheme for velocities. The time step size was set to 0.002 s after ensuring adequate accuracy across all frequency settings investigated.

Our PIV measurements are limited to whole-field (Eulerian) velocity measurements. Hence numerical simulations were used to explore the evolution of passive particle boli under various HFOV scenarios in an effort to quantify convective dispersion over cumulative breathing cycles. To investigate parametrically the influence of HFOV parameters on convective transport in the airway model, the peak Reynolds number was fixed and the product of $V_T \times f$ was held constant; that is, tidal volume and frequency were varied as summarized in Table 2. For adequate comparison of the net particle displacement between the different HFOV scenarios, a total physical time of 6 s was used. Thus, for a frequency of 2 Hz this corresponds to a total of 12 breathing cycles whereas at 10 Hz a total of 60 cycles are simulated.

Lagrangian tracking of passive tracers was implemented using a one-way coupled discrete phase model where an implicit Euler integration scheme was used with an accuracy tolerance of 10^{-5}. Specifically, a total of over 5000 massless particles was initiated in a uniformly spaced cylindrical bolus positioned 20 mm upstream from the first bifurcation, within the trachea. Due to the large tidal volumes pushed in and out during simulations, the airway tree mesh was extended to keep particles from escaping the domain and hence to retain them for ensemble statistics. Due to the planar geometry of the model, each of the eight outlets was extended by adding an identical elbow and a 600 mm long tube (see Fig. 6). At the inlet, the trachea was also extended by 240 mm. All extensions maintained the same diameters as the original boundary conditions and were meshed with hexahedral cells using an O-grid scheme. Subsequent tests on the full extended mesh were performed and results were compared to the non-extended model ensuring no artificial numerical effects were introduced and that ensuing velocities remained within a 0.1% relative discrepancy.

3. Results and discussion

Phase averaged flow patterns are measured by PIV at eight distinct phase angles over a representative oscillatory cycle for CMV (0.5 Hz) and HFOV (5 Hz) conditions, respectively (see scenarios marked with (*) in Table 2). Velocity vectors and corresponding magnitudes are measured in the central x-y plane of the lung model and presented in Figs. 2 and 3 for the inhalation and exhalation phase, respectively. During the inhalation phase, velocity patterns exhibit characteristic skewed velocity profiles across the bifurcating tree as previously observed in adult lung geometries (Adler and Brücker, 2007; Jalal et al., 2016). Such profiles are directly associated with secondary flow structures (i.e. Dean instabilities). Following previous work of Fresconi and Prasad (2007), Dean vortices are typically observed at Dn > 10 in adult bifurcating tree structures. Correspondingly, the resulting Dean numbers in the daughter branches of our neonatal model (see Table 2) are large enough to allow the development of counter rotating vortex structures. While 2D PIV does not allow for direct quantification of the 3D vortex structures, the 2D whole-field velocity maps are thus characterized by the resulting skewness of the velocity profiles. In what

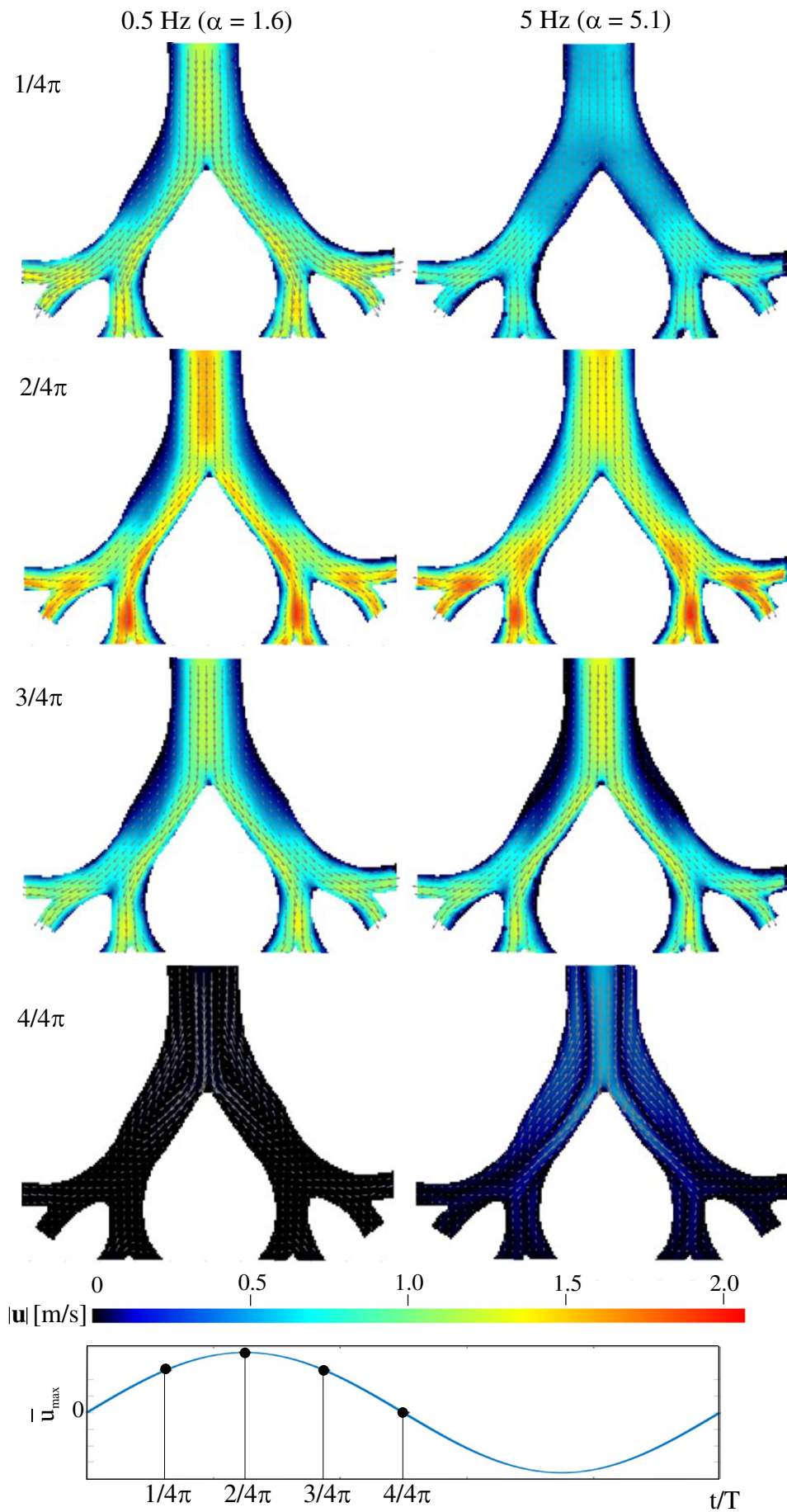## 0.5 Hz (α = 1.6)   5 Hz (α = 5.1)

Fig. 2. Velocity vector maps and corresponding velocity magnitudes from PIV for CMV and HFOV conditions shown at four distinct phase angles during inhalation.
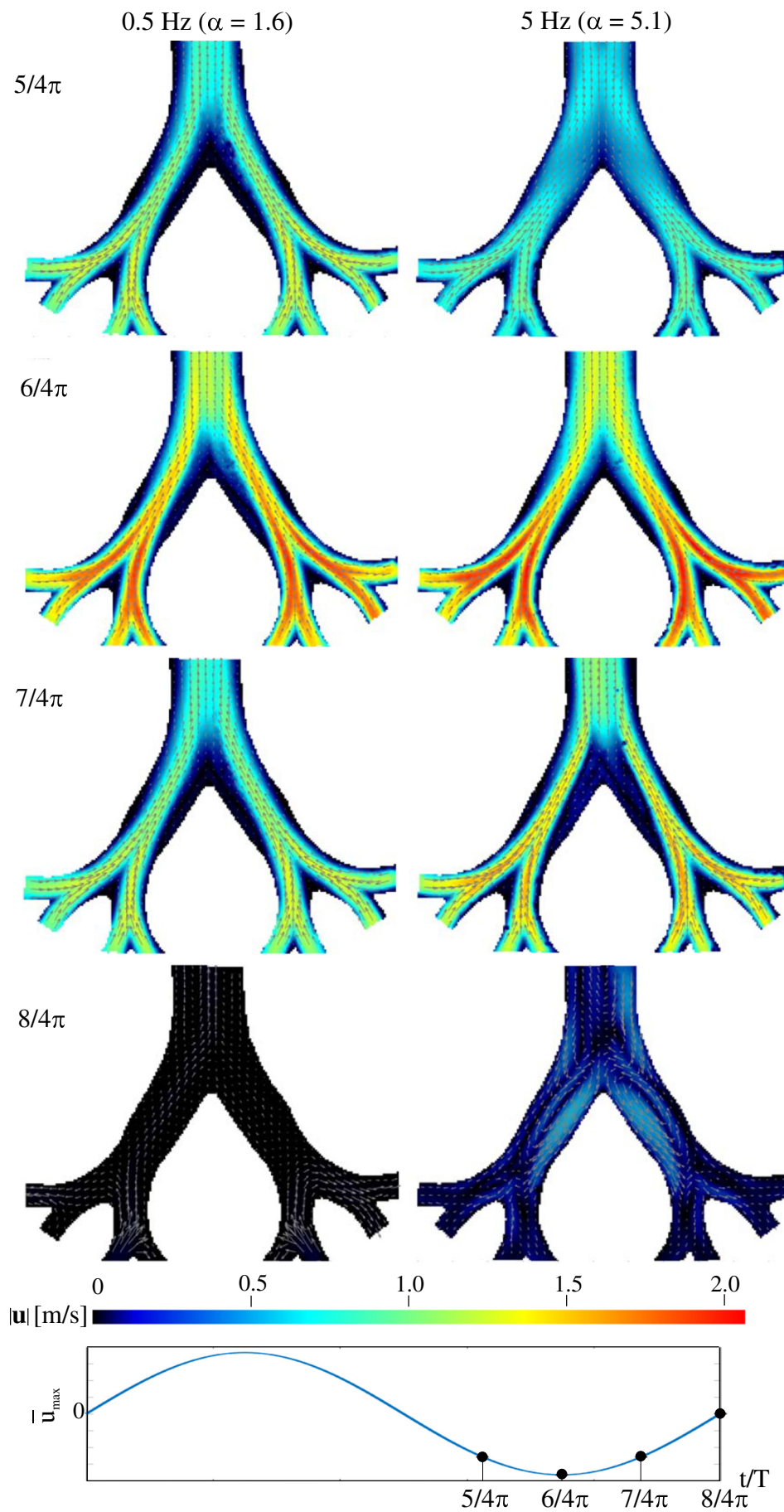
Fig. 3. Velocity vector maps and corresponding velocity magnitudes from PIV for CMV and HFOV conditions shown at four distinct phase angles during exhalation.

follows, we detail the evolution of respiratory flow patterns at characteristic phase angles during the inhalation and exhalation phases.

3.1. Velocity patterns: inhalation

We begin by noting that at the peak inhalation ($t/T = 2/4\pi$; Fig. 2) the overall velocity patterns and magnitudes are strikingly similar between CMV and HFOV. Small local differences can nevertheless be identified in the first daughter generation due to the more parabolic velocity profile in the trachea at 0.5 Hz during peak inhalation; in turn, the velocity peak is more skewed towards the inner walls of the first bifurcation than at 5 Hz, thus leading to higher shear rates and a larger separation zone at 0.5 Hz. During the deceleration phase ($t/T = 3/4\pi$; Fig. 2), the trends appear to flip between low and high frequency. That is, while at 0.5 Hz the radial velocity gradients slightly decrease, a larger separation zone develops at 5 Hz in which a proximal backflow near the outer walls of the main bifurcation may be identified. The large phase shifts between core and near wall flow initiate the occurrence of bidirectional flow this early within the breathing cycle. Such increased local shear rates at higher frequencies might be responsible for augmented cross-sectional mixing and thus convective dispersion under HFOV.

Comparing the acceleration phases at inhalation ($t/T = 1/4\pi$; Fig. 2) for low and high frequencies reveals more pronounced differences. For 0.5 Hz, the velocity pattern is rather identical to that during the deceleration phase ($t/T = 3/4\pi$), discussed above. Namely, a parabolic velocity profile develops in the trachea dominating the flow structure further downstream. Velocity patterns appear to match those at peak inhalation ($t/T = 2/4\pi$), while velocity magnitudes are only scaled. In contrast, during the acceleration phase at 5 Hz the velocity magnitude remains largely constant throughout the main bifurcation; radial velocity gradients are thus significantly lower. This latter pattern is hence distinct from the deceleration phase ($t/T = 3/4\pi$) observed at 5 Hz, although the cross-sectional mean velocity in the trachea is identical for both phase angles.

Perhaps the most striking differences observed between 0.5 Hz and 5 Hz occur at flow reversal ($t/T = 4/4\pi$; Fig. 2), thereby underlining differences between the distinct ventilation scenarios. Although both patterns are characterized by bidirectional flow due to occurring phase shifts between inner and outer wall regions, the overall velocity magnitude at 0.5 Hz is two orders of magnitude smaller than at 5 Hz and hence largely negligible. In contrast, velocity magnitudes reach up to 0.7 m/s at 5 Hz (recalling $V_T \times f$ is constant in both CMV and HFOV) and may thus contribute to mass transport during this short transition.

3.2. Velocity patterns: exhalation

The characteristic similarities and differences observed between CMV and HFOV during the inhalation phase also apply under exhalation (Fig. 3). However, flow patterns during exhalation fundamentally differ from that during inhalation as jet-like flow structures arise from the merging of the flows originating downstream in the daughter branches; a phenomenon that ensues from the onset of the acceleration phase during exhalation ($t/T = 5/4\pi$) and persists throughout the deceleration phase ($t/T = 7/4\pi$). Such characteristic flow topologies have been previously characterized in adult airway tree models (Adler and Brücker, 2007; Choi et al., 2010) and our results confirm to a first degree the general similitude of flow phenomena between neonatal and adult conductive airways. In contrast to inhalation, the influence of airway curvature in giving rise to characteristic Dean vortices is presently reduced; a consequence of the lower local Reynolds number (recalling that Dn $\propto$ Re) along the axial direction of the flows that are observed to merge upstream. As a result, stronger streamwise flows are seen at peak expiration with increased velocity magnitudes ($t/T = 6/4\pi$; Fig. 3), compared to peak inspiration.

In analogy to our discussion during flow reversal at inhalation ($t/$

$T = 4/4\pi$; Fig. 2), we note that during the reversal phase at exhalation ($t/T = 8/4\pi$; Fig. 3) we indeed recover bidirectional flow topologies. Namely, the results for 0.5 Hz reveal a compensational flow between adjacent daughter branches of the same generation; a behaviour that may be attributed to the *pendelluft* phenomenon, although the magnitude is rather low. Interestingly, while velocity magnitudes at this phase angle are significantly higher at 5~ Hz, mass exchange between adjacent branches is not observed. Rather, velocity patterns reveal strong recirculation regions in the main bifurcation. Recalling that *pendelluft* flow is often associated with HFOV (Drazen et al., 1984), our phase-locked results at $t/T = 8/4\pi$ may come short of capturing the existence of *pendelluft* phenomena shortly before and/or after the precise flow reversal instant. Yet, if existent it remains unclear whether such phenomena would create significant convective mixing.

Following our experiments, we briefly return to the original Navier-Stokes equations in their non-dimensional form and attempt to gain qualitative insight into the roles of Re and α on the flow similarities and discrepancies observed between CMV and HFOV. Namely, we recall that

$$\alpha^2 \frac{\partial \mathbf{u^*}}{\partial t^*} + Re\left(\mathbf{u^*} \cdot \nabla^*\right)\mathbf{u^*} = -Re\nabla^* p^* + \nabla^{*2}\mathbf{u^*}, \tag{1}$$

where $\mathbf{u}^*$ is the dimensionless velocity field, t^* the dimensionless time and p^* the dimensionless pressure.

Considering first the flow cycle at peak inhalation, the convective term and hence the influence of the Reynolds number dominates, while the acceleration term is close to zero indicating negligible influence of the Womersley number α. Consequently, similar velocity patterns between CMV and HFOV will appear during peak inhalation (i.e. peak Reynolds number indicated by (*) in Table 2), as observed in experiments ($t/T = 2/4\pi$; Fig. 2). In contrast, at flow reversal the instantaneous Reynolds number approaches zero and thus the convective term is negligible whereas the acceleration term is at its peak and the influence of the Womersley number becomes most pronounced. This supports the strong difference in flow patterns and strength between CMV and HFOV during low velocity phase angles (i.e. $t/T = 4/4\pi$ in Fig. 2 and $t/T = 8/4\pi$ in Fig. 3).

3.3. Numerical simulations

To shed light on the role of velocity patterns towards convective mass transport during HFOV we call on numerical simulations to explore the evolution of boli consisting of passive particle tracers. Given the limitations of the PIV setup, such Lagrangian quantifications would be cumbersome to implement in experiments. We briefly recall that within the scope of the present work our simulations do not consider the coupled effects of convection and diffusion towards gas transport. As a first approximation, this assumption is adequate as the anticipated Peclet numbers (e.g. for oxygen in air) in the neonatal conductive airways are typically much larger than unity, albeit not at time instants near flow reversal.

For validation purposes, CFD results are first compared to PIV measurements. A visual inspection during peak in- and exhalation under HFOV conditions ($f = 5$ Hz, $V_T = 1$ ml) is presented in Fig. 4. Overall, our numerical results are in good agreement with experimental data. Despite such consistency, we do observe that PIV measurements exhibit somewhat more homogeneous velocity profiles at the eight outlets whereas CFD results resemble more parabolic profiles at each outlet. Our PIV measurements are subject to weakened illumination of the tracer particles at the distal ends of the model that leads to lower correlation of particle images. This in turn causes missing velocity information which appears as zero values in the velocity field. In addition, the outlet boundary conditions between experiments and simulations are not strictly identical; while the numerical domain stops short at the outlets as seen in Fig. 4, the outlets of the experimental model are
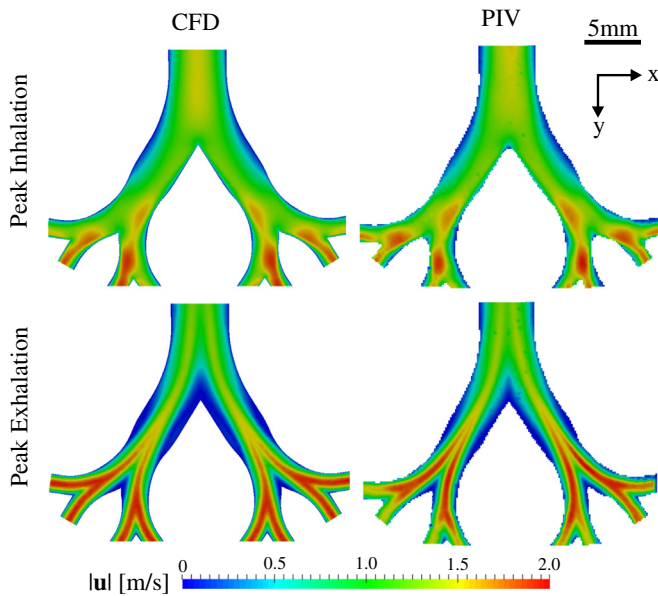
CFD   PIV   5mm

Fig. 4. Comparison of experimental (PIV) and numerical (CFD) results of velocity magnitudes during peak inspiration and expiration.

connected to tubing. Finally, we note that these small discrepancies are seen to disappear upon the addition of the extension tubes at the outlets when exploring convective mass transport (not shown here for brevity), discussed further below.

3.4. Convective mass transport

We exemplify the convective dispersion of the particle bolus under HFOV at 5 Hz in Fig. 5, spanning cumulative breathing cycles up to $t = 6\,T$ (see Supplemental material SM Video 1 for a dynamic rendering of the bolus evolution). At $t = 0$, all particles are coloured grey to identify the initial bolus. Subsequently, particles are shown in red or blue; red denotes a net distal (i.e. positive y-direction) displacement whereas blue indicates a net proximal displacement (i.e. negative y-direction). We recall that the distal ends of the conductive airway model are extended in the orthogonal direction to the x-y plane (i.e. negative z-direction as shown in the inset of Fig. 6). Thus, particles dispersed in the outlet extensions at the end of cycles may be hidden by overlapping particles in the projection of Fig. 5. Nevertheless, these latter particles represent a negligible fraction of the entire bolus ($< 1\%$) and do not weigh on the main conclusions discussed below.

At the end of the first oscillatory cycle ($t = T$), particles have dispersed as far as 7.1 cm ($\sim 13.5 D_0$) in the proximal direction. Notably, the maximal particle displacement at 5 Hz from the point of injection upstream towards the domain inlet is 8.6 cm ($\sim 16.4 D_0$) after 30 cycles (Fig. 6). In other words, within one complete breathing cycle dispersion yields about 80% of the final displacement; after 6 cycles, the net displacement is as high as 98% of the final value. Such rapid asymptotic behaviour may be linked to the limited number of bifurcations and generations of our model. Following seminal studies of Haselton and Scherer (1980), the exchanged volume of a single bifurcation is only 5% of the tidal volume. Here, the dead space captured by the bifurcations of our model is about 1 ml; this region of the domain contributes most to the asymmetric velocity profiles occurring between in- and exhalation (recalling Figs. 2 and 3). Thus, with a tidal volume set at $V_T = 1\,ml$ at 5 Hz the tidal flow crosses through the bifurcating tree during one cycle such that a final net displacement is anticipated within few cycles.

The final bolus distribution after 6 s is shown in Fig. 6 for all frequencies investigated (see Table 2). We note that for the case of 2 Hz particles have travelled upstream by a distance of about 21 cm ($\sim 40 D_0$), whereby the particle concentration gradually decreases with

increasing distance from the injection region with a characteristic "spike" shaped profile at the tip (Henderson et al., 1915). The absence of diffusion in the numerical simulation enhances this sharp profile which would otherwise lead to augmented radial dispersion of the concentration profile while the longitudinal dispersion is impeded by lateral diffusion (Chang, 1984).

Under the assumption of a homogeneous concentration profile, the hypothetical net volume displaced can be estimated. For example, with a peak displacement of about 21 cm upstream of the trachea inlet this hypothetical net volume is $V_{net} \approx 4.6\,ml$ for the case of 2 Hz; note that the real displaced volume is lower. At 4 Hz, the peak displacement and hence the hypothetical volume have exactly halved. For better comparison of the results across all frequencies (2 Hz–10 Hz) the relation V_{net}/V_T yields a fixed value of 1.8 for all cases. This suggests that the net displacement scales linearly with the tidal volume. In turn, lower tidal volumes are not compensated by higher frequencies in terms of achieving a constant net transport behaviour for a fixed $V_T \times f$. Nevertheless, it should be noted that the particle concentration at the profile tips increases with increasing frequency. This might cause a slight deviation from the linear relation between net displaced volume to V_T that cannot be precisely quantified in the current state.

We return to Fig. 6, where each sub-panel is marked by a green octahedron denoting the center of mass of the final bolus across the airway model. We recall that a center of mass positioned exactly at the interface of red and blue particles would denote symmetric proximal and distal particle dispersion. Here instead, we observe that the center of mass is shifted towards the trachea inlet, thus indicating that more particles have travelled upstream in the negative y-direction. As the frequency increases, the distribution of positive/negative displacements becomes more symmetric; a result anticipated as in the limit of infinitely high frequencies, particles would remain still in the absence of diffusion. As discussed above, net convective transport results from asymmetric velocity profiles between in- and expiration (Figs. 2 and 3). In the seminal work of Haselton and Scherer (1980), the authors showed experimentally the dispersion of a dyed fluid bolus reaching well into the distal bifurcating airways of their planar, symmetric model over cumulative breathing cycles; a feature captured in our simulations by the red-coloured particles (Fig. 6). Yet, their experimental setup did not enable the visualization of dye upstream from the inlet such that their conclusions suggested symmetric net transport in both upstream (tracheal) and downstream (bifurcation) directions. Here, the peak expiratory flow patterns differ not only qualitatively but also quantitatively from the peak inspiratory profile, with larger velocity magnitudes in the peak expiration phase. Consequently, a more pronounced and peak-shaped dispersion pattern appears in the upstream section of the trachea; a feature that may somewhat be specific to the setup investigated here. It is anticipated that for a more realistic 3D lung model of the conductive airways net dispersion would develop more symmetrically in the main flow directions.

To quantitatively summarize the results of our ensemble tracking of particles, Fig. 7a presents the mean-square displacement (MSD) at the end of cumulative oscillatory cycles. For all frequencies investigated, the MSDs seem to converge towards a near steady-state value. As anticipated for the lowest tidal volume (0.5 ml at $f = 10\,Hz$), this plateau is rapidly reached within a few cycles. In contrast at $f = 2\,Hz$, the asymptotic behaviour is reached only at the end of the simulation. The absolute values of the MSD are seen to scale in close agreement with the peak tip displacement presented in Fig. 6. We thus remark that despite $V_T \times f$ kept constant, the net displacement decreases linearly with decreasing tidal volume. Moreover, the enhanced counter-flow and increased velocity magnitudes observed for HFOV during the flow reversal phases do not appear to contribute to augmented net mass transport. This may support the hypothesis from previous *in vivo* studies and theoretical models that for neonates ventilation efficiency (Q) follows rather the relation $Q = V_T^2 \times f$ (Pillow, 2005; Courtney et al., 2002; Van de Kieft et al., 2005), emphasizing the greater importance of
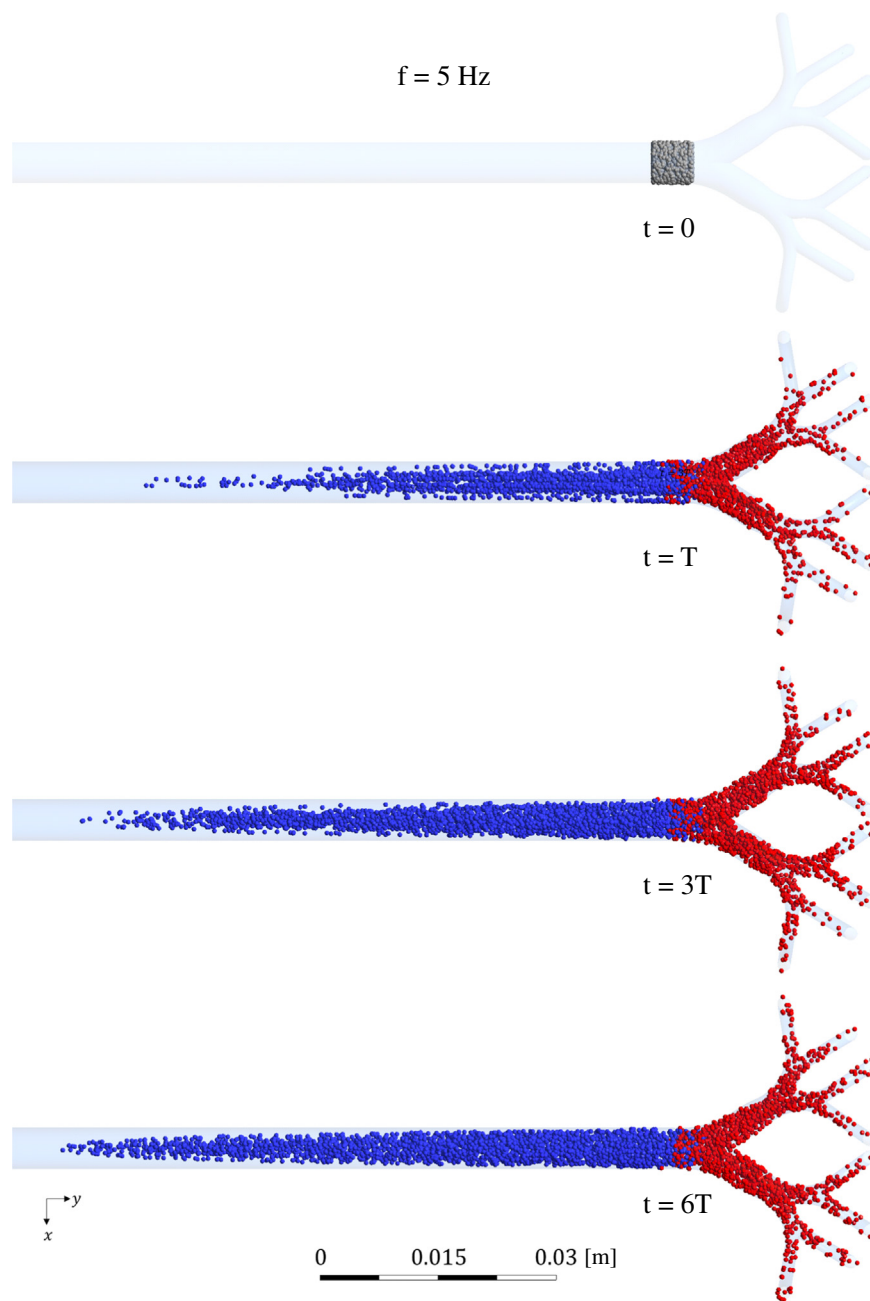
Fig. 5. Initial particle distribution of the bolus at $t = 0$ and at the end of exhalation after 1, 3 and 6 breathing cycles as exemplified for the case of 5 Hz. (For interpretation of the references to colour in this figure, the reader is referred to the web version of this article.)

tidal volume relative to frequency; a point to be addressed in the future.

Finally, Fig. 7b quantifies the fraction of particles subject to net positive *y*-motion at the end of each cycle. For the lower frequencies (i.e. 2 Hz–5 Hz), the ratio is well below 0.5 and suggests somewhat an asymptotic behaviour towards a stead-state value. With increasing frequency (and thereby decreasing tidal volume), the net displacement of the bolus is more homogeneously distributed between proximal and distal directions within the lung model. Indeed, for the largest frequency (10 Hz) this ratio is fairly balanced where the asymptotic behaviour suggests a near 0.5 value as seen earlier from the identification of the center of mass (Fig. 6). It is hypothesized that with higher oscillatory frequencies under HFOV the specificities of the conductive airway anatomy (e.g. bifurcations) will thus play a lesser role relative to the imposed frequency in determining this net convective transport.

4. Conclusion

In the present work, we have attempted to shed new light on the mechanistic underpinnings of convective mass transport in an anatomically-inspired model of neonatal conductive airways. Despite the limitations of our *in vitro* and *in silico* approaches, our findings suggest that to a good approximation flow phenomena are strikingly similar between HFOV and CMV as further supported by basic dimensionless analysis. In the absence of diffusional transport, our results contrast with the often widespread understanding that transport mechanisms in HFOV fundamentally differ from those in CMV. Specifically, we find that net convective transport scales linearly with the applied tidal volume. Although velocity patterns are characterized by phase angle dependent differences, these are anticipated to play a small role in significantly altering convective mass transport mechanisms. Hence, opting for lower tidal volumes to reduce the risks of lung injury (i.e. baro- and volutrauma) in clinical HFOV settings must be carefully
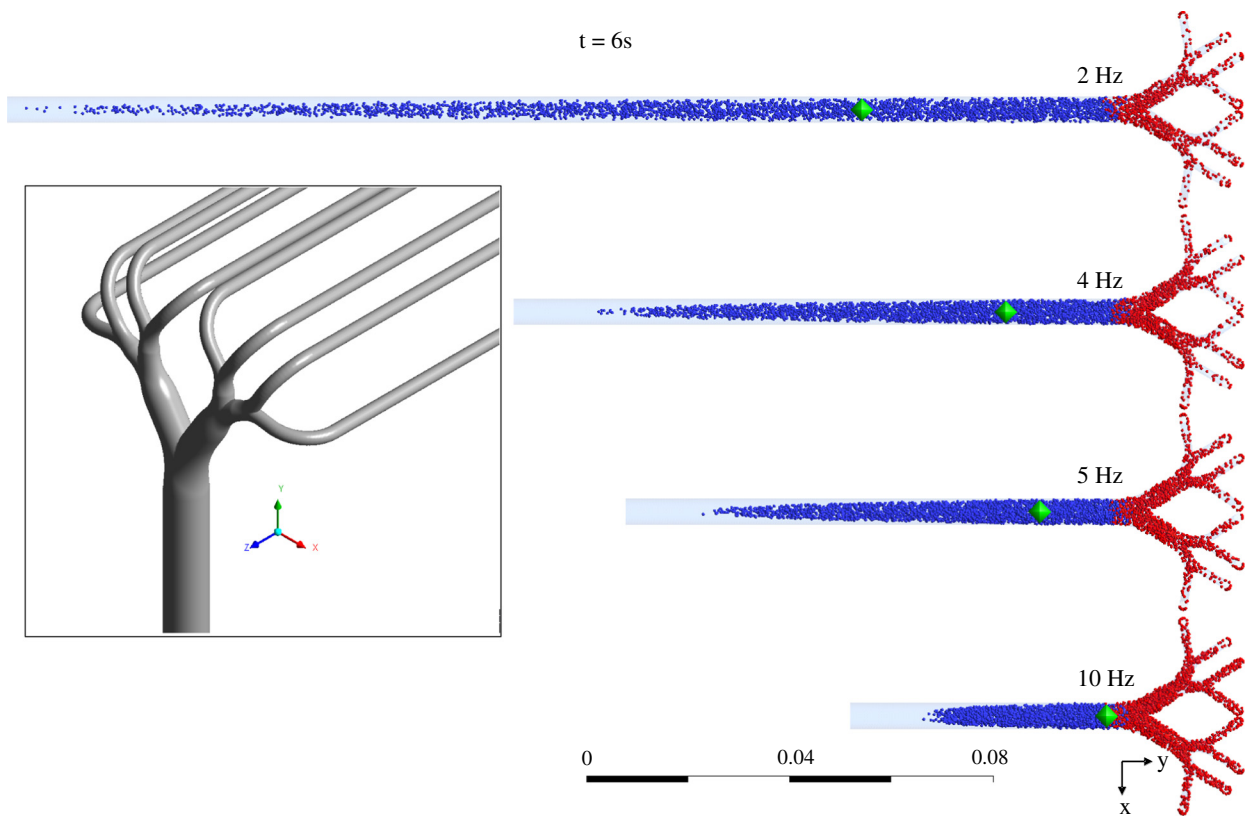
Fig. 6. Net convective displacements of the bolus under various HFOV settings at the end of exhalation for cumulative breathing cycles at $t = 6$ s. Inset: details of the model geometry. (For interpretation of the references to colour in this figure, the reader is referred to the web version of this article.)

selected to guarantee sufficient ventilation efficiency.

It is important to bear in mind that the results presented here are restricted to assessing a fixed (peak) Reynolds number and thus maintaining the product $V_T \times f$ constant. Indeed, it remains to be explored how the relationship $V_T^2 \times f$ might modulate net convective transport and thus ventilation efficiency, as previously suggested (Pillow, 2005). This is subject to further investigation.

Supplementary data to this article can be found online at http://dx.doi.org/10.1016/j.clinbiomech.2017.11.009.
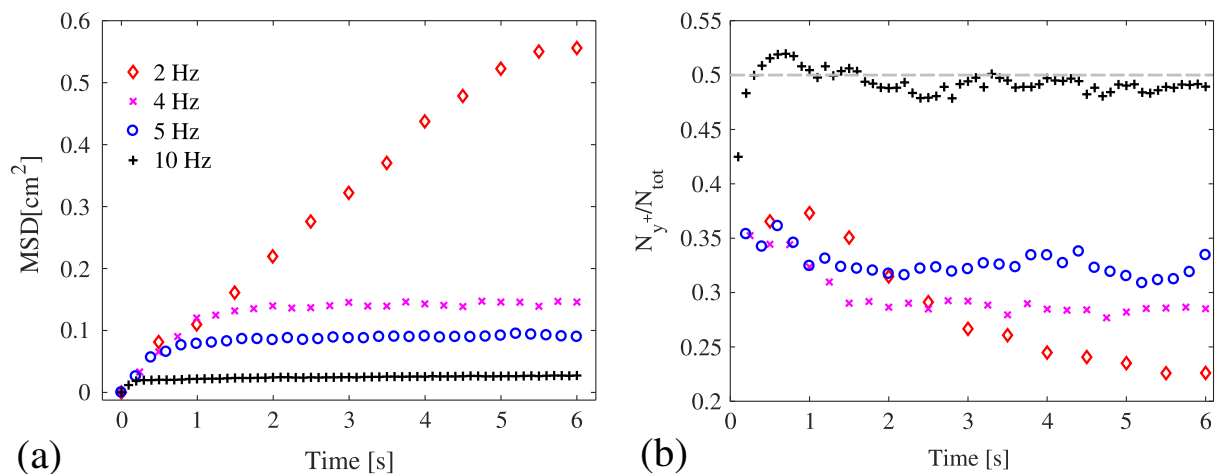
Fig. 7. (a) Mean square displacement (MSD) for frequencies ranging from 2 Hz to 10 Hz. (b) Corresponding ratio of particles with pure positive y-displacement (N_y+) to the total number of particles N_{tot} over cumulative breathing cycles.

References

Adler, K., Brücker, C., 2007. Dynamic flow in a realistic model of the upper human lung airways. Exp. Fluids 43 (2-3), 411–423.

Bauer, K., Rudert, A., Brücker, C., 2012. Three-dimensional flow patterns in the upper human airways. J. Biomech. Eng. 134 (7) 071006–1-9.

Chang, H.K., 1984. Mechanisms of gas transport during ventilation by high-frequency oscillation. J. Appl. Physiol. (Bethesda, Md.: 1985) 56 (3), 553–563.

Choi, J., Xia, G., Tawhai, M.H., Hoffman, E. a., Lin, C.L., 2010. Numerical study of high-frequency oscillatory air flow and convective mixing in a CT-based human airway model. Ann. Biomed. Eng. 38 (12), 3550–3571.

Courtney, S.E., Durand, D.J., Asselin, J.M., Hudak, M.L., Aschner, J.L., Shoemaker, C.T., 2002. High-frequency oscillatory ventilation versus conventional mechanical ventilation for very-low-birth-weight infants. N. Engl. J. Med. 347 (9), 643–652.

De Luca, D., Dell'Orto, V., 2016. Non-invasive high-frequency oscillatory ventilation in neonates: review of physiology, biology and clinical data. Arch. Dis. Child. Fetal Neonatal Ed. 101 (6), F565–F570.

Drazen, J., Kamm, R.D., Slutsky, A., 1984. High-frequency ventilation. Physiol. Rev. 64 (2), 505–543.

Fresconi, F.E., Prasad, A.K., 2007. Secondary velocity fields in the conducting airways of the human lung. J. Biomech. Eng. 129 (5), 722–732.

Gerstmann, D.R., Wood, K., Miller, A., Steffen, M., Ogden, B., Stoddard, R.A., Minton, S.D., 2001. Childhood outcome after early high-frequency oscillatory ventilation for neonatal respiratory distress syndrome. Pediatrics 108 (3), 617–623.

Große, S., Schröder, W., Klaas, M., Klöckner, A., Roggenkamp, J., 2007. Time resolved analysis of steady and oscillating flow in the upper human airways. Exp. Fluids 42 (6), 955–970.

Han, B., Hirahara, H., Yoshizaki, S., 2016. Streaming caused by oscillatory flow in peripheral airways of human lung. Open J. Fluid Dynamics 06 (03), 242–261.

Haselton, F., Scherer, P., 1980. Bronchial bifurcations and respiratory mass transport. Science 208 (4), 69–71.

Haselton, F.R., Scherer, P.W., 1982. Flow visualization of steady streaming in oscillatory flow through a bifurcating tube.pdf. J. Fluid Mech. 123, 315–333.

Henderson, Y., Chillingworth, F.P., Whitney, J.L., 1915. The respiratory dead space. Amer. J. Physiol. 38, 1–19.

Imai, Y., Nakagawa, S., Ito, Y., Kawano, T., Slutsky, a. S., Miyasaka, K., 2001. Comparison of lung protection strategies using conventional and high-frequency oscillatory ventilation. J. Appl. Physiol. 91 (4), 1836–1844.

Jalal, S., Nemes, A., de Moortele, T.V., Schmitter, S., Coletti, F., 2016. Three-dimensional inspiratory flow in a double bifurcation airway model. Exp. Fluids 57 (148), 11.

Kamm, R.D., 1989. Toward improved methods of high frequency ventilation: a study of gas transport mechanisms. Acta Anaesthesiol. Scand. 33 (s90), 51–57 Sep.

Ménache, M.G., Hofmann, W., Ashgarian, B., Miller, F.J., 2008. Airway geometry models of children's lungs for use in dosimetry modeling. Inhalation Toxicol. 20 (2), 101–126 Jan.

Nieman, G.F., Satalin, J., Kollisch-Singule, M., Andrews, P.L., Aiash, H., Habashi, N.M., Gatto, L.A., 2017. Physiology in Medicine: Understanding dynamic alveolar physiology to minimize ventilator induced lung injury (VILI). J. Appl. Physiol. 1 jap.00123.2017.

Otis, A.B., McKerrow, C.B., Bartlett, R.A., Mead, J., McIlroy, M.B., Selver-Stone, N.J., Radford, E.P., 1956. Mechanical factors in distribution of pulmonary ventilation. J. Appl. Physiol. (Bethesda, Md.: 1985) 8 (4), 427–443.

Owen, L.S., Manley, B.J., Davis, P.G., Doyle, L.W., 2017. The evolution of modern respiratory care for preterm infants. Lancet 389 (10079), 1649–1659.

Pillow, J.J., 2005. High-frequency oscillatory ventilation: mechanisms of gas exchange and lung mechanics. Crit. Care Med. 33 (3), S135–S141.

Rimensberger, P.C., Schulzke, S.M., Tingay, D., Von Ungern-Sternberg, B.S., 2015. Pediatric and Neonatal Mechanical Ventilation.

Slutsky, A.S., Drazen, J.M., 2002. Ventilation with small tidal volumes. N. Engl. J. Med. 9 (347), 630–631.

Slutsky, A.S., Ranieri, V.M., 2013. Ventilator-induced lung injury. N. Engl. J. Med. 369 21126–2136.

Stachow, R., 1995. High-Frequency Ventilation Basics and Practical Applications.

Tanaka, G., Oka, K., Tanashita, K., 2001. Secondary flow augmentation during intermittent oscillatory flow in model human central airways. JSME Int. J., Ser. C 44 (4), 1041–1050.

Theunissen, R., Riethmuller, M.L., 2008. Particle image velocimetry in lung bifurcation models. Topics Appl. Physics 112, 73–101.

Van de Kieft, M., Dorsey, D., Morison, D., Bravo, L., Venticinque, S., Derdak, S., 2005. High-frequency oscillatory ventilation: lessons learned from mechanical test lung models. Crit. Care Med. 33 (3 Suppl), S142–S147.

Venegas, J., Fredberg, J., 1994. Understanding the pressure cost of ventilation — why does high-frequency ventilation work? Crit. Care Med. 22 (9), 49–57.

Whitehead, T., 2002. The pulmonary physician in critical care: ventilator induced lung injury. Thorax 57 (7), 635–642.